Journal of Quantitative Spectroscopy & Radiative Transfer 134 (2014) 91–103

Contents lists available at ScienceDirect

Journal of Quantitative Spectroscopy & Radiative Transfer

journal homepage: www.elsevier.com/locate/jqsrt

Scattering properties of soot-containing particles and their impact by humidity in 1.6 μm

M. Fan [a,b], L. Chen [a,*], X. Xiong [c], S. Li [a,d], J. Tao [a], L. Su [a], M. Zou [a,b], Y. Zhang [a]

[a] State Key Laboratory of Remote Sensing Science, Institute of Remote Sensing and Digital Earth, Chinese Academy of Sciences, Beijing 100101, China
[b] University of Chinese Academy of Sciences, Beijing 100049, China
[c] Center for Satellite Applications and Research (STAR), National Environmental Satellite, Data, and Information Service (NESDIS), NOAA, College Park, MD 20740, USA
[d] Rollins School of Public Health, Emory University, Atlanta, GA 30322, USA

ARTICLE INFO

Article history:
Received 6 May 2013
Received in revised form
8 November 2013
Accepted 9 November 2013
Available online 19 November 2013

Keywords:
Scattering properties
Relative humidity
Soot-containing particle
T-matrix method
CMGMM

ABSTRACT

Short-wave infrared (SWIR) band in wavelength near 1.6 μm is one of the key bands used for satellite observation of Carbon Dioxide (CO_2). However, one major uncertainty to use this band for the CO_2 retrieval is the scattering by cloud and aerosol particles. To better understand the scattering properties of soot-containing particles in this band, this paper studied the scattering properties for three typical types of soot-containing particles in China: (I) internal mixture, (II) pure soot aggregate, and (III) semi-external mixture. Assumed as single non-spherical particle for type I, its scattering property is computed using the T-matrix method combined with the Maxwell–Garnett effective medium theory and the hygroscopic growth theory. For types II and III, a particle-cluster aggregation algorithm is employed to generate fractal-like aggregates, and their scattering properties are computed using the Core–Mantle Generalized Multi-sphere Mie-solution method combined with the hygroscopic growth theory of both monomers and aggregated particles. The simulated results demonstrate that their scattering properties are quite different and strongly impacted by the levels of relative humidity (RH). For type I, the RH plays a much more important role than the morphology in impacting the scattering properties, and the scattering phase functions among different shaped particles have a larger difference for larger particles and higher RH. For type II, both the RH and morphology significantly affect its scattering properties. The single scattering albedo (ω) can be underestimated up to ~50% without considering the effects of RH and morphological changes. For type III, its scattering properties mainly depend on the RH and the size of the large water-soluble particle. Although the enlarged soot aggregate, which is attached to a water-soluble particle, almost does not change the light direction, it can result in a significant reduction in ω (~0.15) at low RH for small particles. By comparing the scattering parameters of wet particles at a certain RH level with the dry ones, the impact by the heterogeneity of aerosols generally becomes larger with the increase of RH, but becomes smaller with the increase of particle size. These results suggest that, although the water vapor absorption itself is small in 1.6 μm CO_2 band, it can significantly impact the scattering properties of these particles through its effect on the hygroscopic growth of the non-spherical and heterogeneous aerosols. This impact should be taken into account in the retrieval of CO_2 using 1.6 μm as well as other related remote sensing applications.

* Correspondence to: State Key Laboratory of Remote Sensing Science, Institute of Remote Sensing and Digital Earth, Chinese Academy of Sciences, P.O. Box 9718, No. 20 Datun Road, Olympic Science & Technology Park of CAS, Beijing 100101, China. Tel.: +86 1581115013, +86 64836589.
E-mail address: lfchen@irsa.ac.cn (L. Chen).

0022-4073/$ - see front matter © 2013 Elsevier Ltd. All rights reserved.
http://dx.doi.org/10.1016/j.jqsrt.2013.11.004

1. Introduction

As space-based remote sensing has an advantage of providing a huge number of CO_2 measurements on a regional or global scale, satellite retrieval results of the CO_2 column-average dry air mole fractions (XCO_2) have the potential to be used as a constraint for inverse modeling to derive CO_2 fluxes across the surface–atmosphere boundary, which in turn will foster insight into the related biogeochemical cycles [1,2]. The weak CO_2 band near 1.6 μm is selected as the primary candidate for CO_2 measurement because it is relatively free of absorption by other gases, and few of the spectral lines in this band saturates by CO_2 absorption even at high solar zenith angles [3–5]. However, one challenge for the satellite measurements of XCO_2 using this SWIR wavelength range is the impact of multiple scattering by aerosols, which could result in large errors on the retrieved XCO_2 [6–8]. As a large source of anthropogenic aerosols as well as CO_2 emission, China is experiencing a rapid development of industrialization during the last three decades. More and more frequent severe brown haze episodes have been observed in recent years [9–11], and it was found that the primary contributors to the haze formation are carbonaceous soot, secondary aerosol formation and their hygroscopic growth, which strongly depend on the RH of the ambient air [12–15]. Since the semi-external and internal mixtures of soot with other aerosol components (e.g. inorganic water-soluble particles) in the atmosphere could impact the light transfer in 1.6 μm CO_2 band, an accurate retrieval of CO_2 using SWIR band in China needs to pay more attention to accurately estimate the scattering properties of soot-containing particles, as well as their impact by the RH in this band.

Aerosols are usually assumed to be spherical and homogeneous particles in many climate and remote sensing applications, thus their optical properties can be easily computed using the Mie scattering [16,17]. However, several studies using transmission electron microscopy (TEM) on the size distribution, morphology and chemical compositions of particles collected during some haze events in China found that most particles have irregular shapes and are heterogeneous [18–21]. For example, Li et al. [19] conducted sample collections during brown haze episodes in Beijing, northern China, and their TEM observations showed that approximately 90% of the collected particles were covered by visible coatings. Moreover, soot and soot-containing aggregated particles are commonly formed due to biomass burning and fuel combustion, which actually contain ten to hundreds of tiny, nearly spherical particles. Hence an assumption of non-spherical and heterogeneous aerosols is more appropriate and should be used in computing their optical properties.

For irregularly shaped aerosols, like single non-spherical particles and the fractal-like aggregates, various methods have been developed and applied for calculating their scattering properties. The scattering parameters of single non-spherical particles can be calculated by solving electromagnetic equations with rigorous methods, such as the T-matrix method [22–25], the finite difference time domain (FDTD) method [26,27] and the discrete dipole approximation (DDA) method [28]. The T-matrix method will be used in this study because of its high efficiency and accuracy, especially for symmetric particles. Two methods have ever been used to compute the scattering properties of fractal-like aggregates, one is the Rayleigh–Debye–Gans (RDG) theory [29], and the other is the coupled electric and magnetic dipole (CEMD) method [30]. However, these two methods, especially the RDG theory, are not accurate enough to verify the scattering characteristics of particle clusters because the multiple scattering within the aggregates has not been taken into account. On the basis of the work by Bruning and Lo [31,32], two more accurate methods have been developed to compute the radiative properties of aggregates formed by non-overlapping spherical particles, one is the cluster T-matrix method (CMT) [33,34] and the other is the generalized multi-sphere Mie-solution (GMM) [35,36]. One significant difference between them is that the GMM straightly manages precise phase relations of both incident and scattered waves, while the CTM expresses both phase factors in terms of infinite series expansions. Compared to the CTM, GMM can handle a wider range of ensemble-sizes [37]. Moreover, Xu and Khlebtsov [37] used an improved GMM method to directly compute the scattering properties of the aggregates with coated inhomogeneous monomers, which is referred to as the core–mantle GMM (CMGMM) method, and this method will be used for aggregated particles in this study.

For the heterogeneous aerosols, especially for the single internally mixed particles, a difficulty in the simulation of their scattering properties is how to determine their effective complex refractive indices. Three effective medium rules widely used are the Maxwell–Garnett (MG) rule [38,39], the Bruggeman rule [40,41] and the coherent potential approximation (CPA) rule [42,43]. By calculating the effective permittivities of the mixed particles using these mixing rules, we can obtain the effective complex refractive indices. As the MG rule is independent on the size of the inclusions, it is more suitable to the mixtures whose inclusions have arbitrary shapes. The Bruggeman rule is symmetric with respect to the influence by the inclusion and its environment. And the CPA rule assumes a full coupling between neighboring inclusions, and the background permittivity is equal to the permittivity of the mixture. It is found by Liu [44] that for water-coated aggregates, the MG rule performed better than the Bruggeman rule over a wide range of water coating thicknesses and cluster sizes.

Based on the hygroscopic growth theory and the TEM images of soot-containing aerosol particles from the brown hazes in China, we considered the aerosols with both the single non-spherical particles and the aggregates and computed their scattering properties, with a focus on the influence to these properties from RH in this study. For the single non-spherical particles, the scattering parameters are calculated by combining the T-matrix method and the MG effective medium rule. For the fractal-like aggregated particles, a diffusion-limited particle-cluster aggregation algorithm is firstly used to generate the aggregates with different monomer numbers, morphological structures and sizes of spherical monomers, and then

the CMGMM method is used for computing their scattering parameters. Section 2 describes the methods and the models to simulate three types of soot-containing aerosols and compute the optical properties. The results of the simulated scattering properties and their relation with RH will be given in Section 3. Section 4 is a summary and conclusions.

2. Method and model

2.1. Generation of fractal-like aggregates

As mentioned above, many aggregated soot aerosols with complex structures cannot be successfully approximated as simple irregular shapes. The fractal-like nature of such aggregates can be mathematically expressed through the following statistical scaling law [45,46]:

$$N = k(R_g/a_{drop})^{D_f} \tag{1}$$

where a_{drop} is the mean radius of spherical monomers (assumed constant), k is the fractal prefactor, D_f is the fractal dimension, N is the monomer number of the aggregate, and R_g is the radius of gyration. The usual R_g is defined via the mean square of the distances between the spherical monomer centers and the geometrical center of mass of the aggregate.

In this study, the sequential algorithm (SA) developed by Filippov et al. [46] is selected. It is a tunable particle-cluster aggregation method, where identical spherical monomers are added iteratively, and each step exactly satisfies the scaling law (Eq. (1)) for the fixed fractal dimension and prefactor. From the step $N-1$ to N, the center position $\mathbf{r}_N$ of the Nth monomer must be situated on the surface of the currently existed aggregate determined by the equation:

$$(\mathbf{r}_N - \mathbf{r}^0_{N-1})^2 = \frac{N^2a^2}{N-1}\left(\frac{N}{k}\right)^{2/D_f} - \frac{Na^2}{N-1} - Na^2\left(\frac{N-1}{k}\right)^{2/D_f} \tag{2}$$

where $\mathbf{r}^0_{N-1}$ is the center of mass of the first $N-1$ monomers. As long as the new monomer is placed randomly at the surface of the current aggregate with the restrictions of not overlapping and having at least one contact point with the previously attached $N-1$ monomers, the procedure repeats for the next attaching monomer.

2.2. Models of effective medium and hygroscopic growth

For the single non-spherical particles, the MG rule is employed to obtain the equivalent optical constants of complex heterogeneous particles, which is defined as follows:

$$\varepsilon_{eff} = \varepsilon_{drop} + \frac{3f\varepsilon_{drop}(\varepsilon_{incl} - \varepsilon_{drop})}{\varepsilon_{incl} + 2\varepsilon_{drop} - f(\varepsilon_{incl} - \varepsilon_{drop})} \tag{3}$$

where the permittivities of the inclusion and its environment (drop) are denoted by ε_{incl} and ε_{drop}, respectively. f is the volume fraction of the inclusions, and ε_{eff} is the effective permittivity of the composite. Based on the interconversion of permittivity and complex refractive index, the ε_{incl} and ε_{drop} are initially derived from the complex refractive indices of inclusion and its environment, respectively. The ε_{eff} can be calculated by Eq. (3), and then it will be converted into the effective complex refractive index as an input parameter for the T-matrix method.

Most ambient aerosol particles experience a diameter hygroscopic growth with increasing RH, which can be approximately simulated using the hygroscopic growth theory. The hygroscopic growth factor (GF) at a certain RH is defined as the ratio of the diameter of a humidified particle to that of the corresponding dry one (RH=0%). Here, the empirical γ-model [47–50] is employed to describe the hygroscopic growth of ambient aerosol particles, and a correction factor is introduced after considering the differences between the modeled GF and the experimental results [51]. The two-parameter functional form is shown as follows:

$$\mathrm{GF} = \alpha(1 - \mathrm{RH}/100)^{-\gamma} \tag{4}$$

where γ is the model parameter, and α is the correction factor. In this study, we assume that the sizes of hydrophobic inclusions of soot-containing particles (or the monomers of aggregates) do not change, except the thickness of hygroscopic shells varies with RH. The shell thickness is set as 0 for dry air with a RH of 0%.

2.3. T-matrix method

The T-matrix method originally developed by Waterman [22] is used to calculate the scattering properties of single non-spherical particles in this study. Owing to the linearity of Maxwell's equations and boundary conditions, the relation between the scattered field coefficients p_{mn} and q_{mn} and the incident field coefficients a_{mn} and b_{mn} must be linear and can be expressed by a transition matrix (T matrix) $\mathbf{T}$ as follows [22–25]:

$$p_{mn} = \sum_{n'=1}^{\infty}\sum_{m'=-n'}^{n'}[T^{11}_{mnm'n'}a_{m'n'} + T^{12}_{mnm'n'}b_{m'n'}] \tag{5}$$

$$q_{mn} = \sum_{n'=1}^{\infty}\sum_{m'=-n'}^{n'}[T^{21}_{mnm'n'}a_{m'n'} + T^{22}_{mnm'n'}b_{m'n'}] \tag{6}$$

Eqs. (5) and (6) can be rewritten as

$$\begin{bmatrix}\mathbf{p}\\ \mathbf{q}\end{bmatrix} = \mathbf{T}\begin{bmatrix}\mathbf{a}\\ \mathbf{b}\end{bmatrix} = \begin{bmatrix}\mathbf{T}^{11} & \mathbf{T}^{12}\\ \mathbf{T}^{21} & \mathbf{T}^{22}\end{bmatrix}\begin{bmatrix}\mathbf{a}\\ \mathbf{b}\end{bmatrix} \tag{7}$$

Eq. (7) is the basis of the T-matrix method. If the T matrix for a given scatter is known, the scattered field can be computed easily, as a_{mn} and b_{mn} of the incident plane wave can be simply calculated using closed-form analytical expressions. Consequently, the amplitude matrix can be obtained.

2.4. Core–mantle Generalized Multi-sphere Mie-solution (CMGMM) method

Due to the interaction and far-field interference among scattered waves from individual particles, scattering properties of an aggregate may differ significantly from those of a single particle. By combining the GMM method with the core–mantle sphere Mie theory, the CMGMM method rigorously accounts for the multiple scattering within the aggregate, and provides a strict and complete solution to

the lighting scattering problems of core–mantle fractal-like aggregates. The key steps include (1) expending the scattered, internal, and incident electromagnetic fields in terms of spherical vector wave functions, (2) forming the partial scattered field at each monomer in the aggregate and establishing a large-dimensional linear system derived from the boundary condition, (3) using the addition theorems to transform the waves scattered by an individual monomer into the incident waves of other monomers of the aggregate, and (4) solving for the scattering interactive coefficients in the linear system by an asymptotic iteration method. The amplitude scattering matrix was given by Xu [37]. The CMGMM method can also be applied to the aggregated particle containing irregularly homogeneous monomers, in which the T-matrix method is used to calculate the T-matrices of these monomers in the overall particle reference system.

2.5. Particle types and complex refractive indices used in simulation

Because the TEM gives a resolution less than nanometer scale, many previous studies have used the TEM to investigate the detailed information on size, composition, morphology, and mixing state of soot-containing particles collected in China during brown haze/fog episodes [18–21]. According to these previous TEM analyses, we grouped atmospheric soot-containing particles from China into three typical types, as shown in Table 1 and Fig. 1. Type I particle is defined as the soot particle encapsulated by water-soluble (nitrate and/or sulfuric) coating (Fig. 1(a) and (b)). Type II particle is the pure soot aggregate (Fig. 1(c)), and type III particle is the soot aggregate semi-externally mixed with other relatively large water-soluble particle (Fig. 1(d)). Fig. 2 displays five examples of type I particles (Fig. 2(a)–(e)), and aggregate realizations of type II (Fig. 2(f)–(k)) and type III (Fig. 2(l)) particles simulated using the sequential algorithm.

The complex refractive indices at 1.6 μm (Table 2) used for scattering property simulations are obtained via interpolation from the following two databases: Optical Properties of Aerosols and Clouds (OPAC) package [52] and HITRAN2008 database [53]. Here, both the coating of the type I particle and the extra particle of type III are treated as the water-soluble material, which usually originates from the gas to particle conversion and consists of various kinds of sulfates, nitrates, organic, and other water-soluble substances [52]. The OPAC package supplies the refractive indices of water-soluble component with RH between 0% and 95%.

3. Results and discussion

3.1. Soot with water-soluble coating (type I particle)

The coefficients of GF model (Eq. (4)) for type I particles are taken from the study of Hanel [54] where $\gamma=-0.25$ and $\alpha=1$. It can be expressed

$$\mathrm{GF}_{type\ I}=R_{wet}/R_{dry}=R_{drop}/R_{incl}=(1-\mathrm{RH}/100)^{-0.25} \quad (8)$$

where R_{wet} is the wet particle radius, R_{dry} is the dry particle radius, R_{incl} is the radius of hydrophobic inclusion, and R_{drop} is the radius of the entire individual drop. $R_{wet}=R_{drop}$ and $R_{dry}=R_{incl}$, because we assume that the radius of the

Table 1
Classification criteria for different soot-containing particle groups.

Particle groups	Particle types	Physical characteristics of particles
Type I	Internal mixture	a. No distinct shapes, sensitive to strong electron beam; b. Soot aggregates embedded by complex secondary particles.
Type II	Pure soot	a. Chain-like aggregates.
Type III	Semi-external mixture	a. No distinct shapes, sensitive to strong electron beam; b. Soot aggregates semi-externally mixed with other relatively large particles.

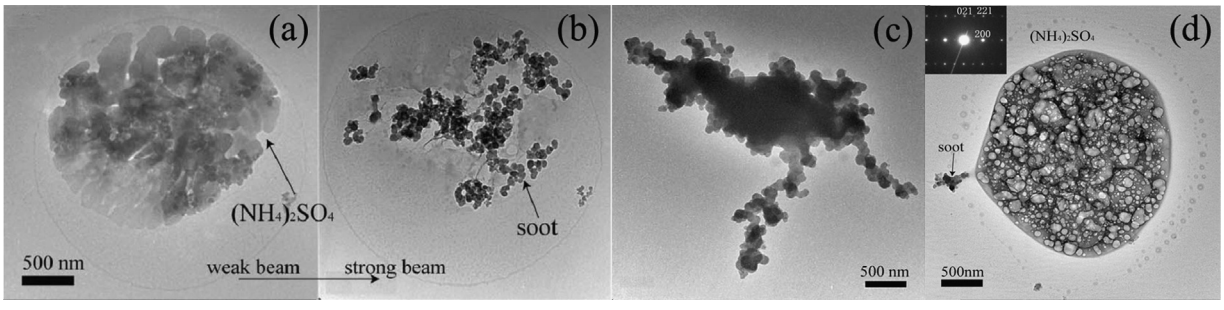

Fig. 1. TEM images of aerosol particles collected from China during haze events [18–21]. (a) A $(NH_4)_2SO_4$ particle in the weak electron beam, (b) soot coated with $(NH_4)_2SO_4$ in the strong electron beam, (c) soot aggregate, and (d) a $(NH_4)_2SO_4$ particle semi-externally mixed with soot aggregate.

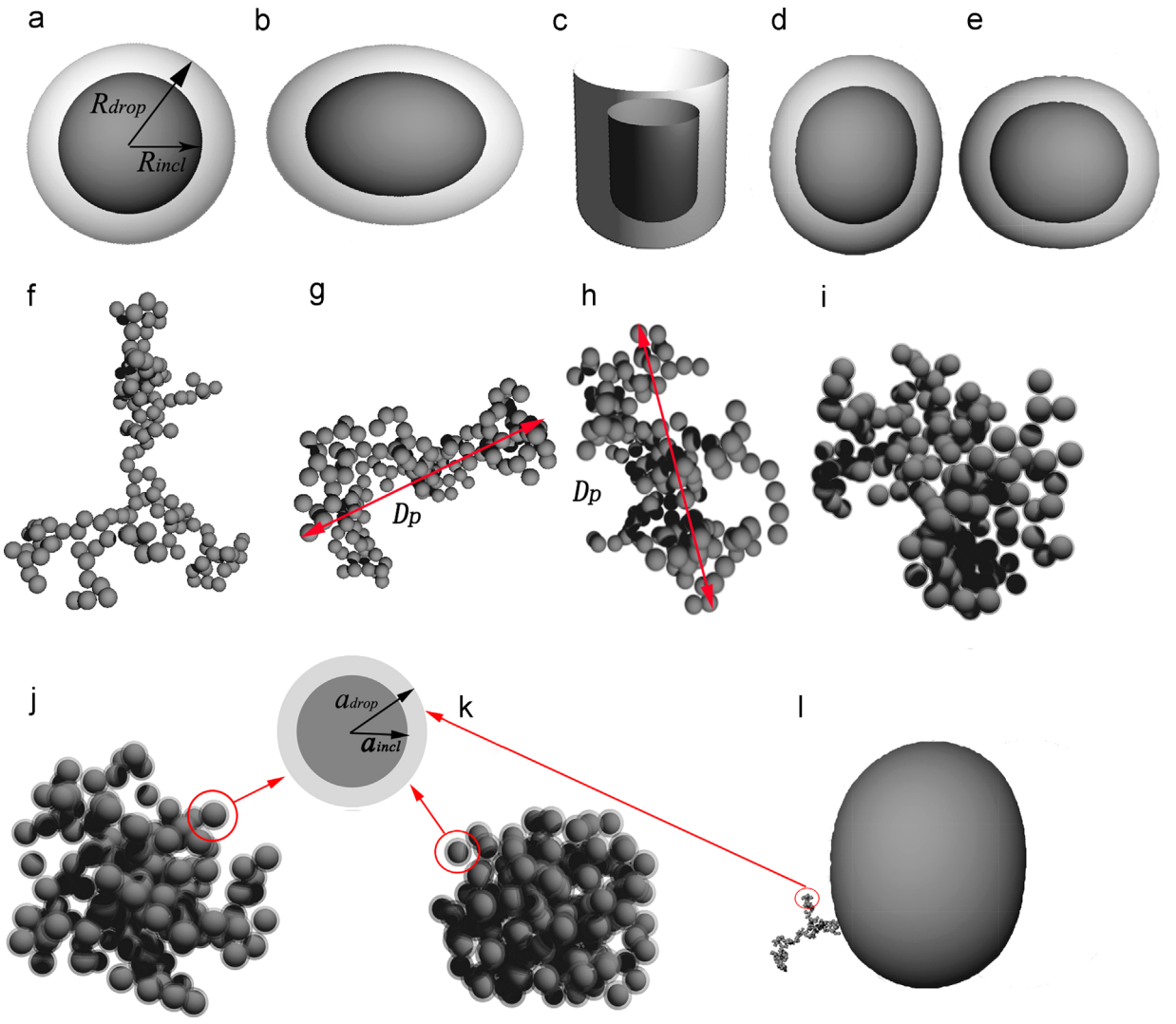

Fig. 2. Simulated soot-containing particles. (a)–(e) Coated single particles. (a) and (b) Spheroids with axial ratio $a/b=1$and 2, respectively; (c) cylinder with diameter/height ratio $D/L=1$; (d) and (e) Chebyshev particles with polynomial of degree $n=2$ and deformation parameter $\varepsilon=0.1$ and -0.1, respectively. (f)–(k) Fractal-like soot aggregates with $N=150$ monomers and characterized by $k=1.19$ with different values of $D_f=1.82$, 1.91, 2.09, 2.21, 2.43 and 2.7 for corresponding RH=0%, 50%, 70%, 80%, 90% and 95%, respectively. (l) Soot aggregate ($k=1.19$, $D_f=1.82$, $N=150$) semi-externally mixed with an extra Chebyshev particle ($n=2$ and $\varepsilon=0.1$). (For interpretation of the references to color in this figure, the reader is referred to the web version of this article.)

Table 2
Complex refractive indices of soot, water and water-soluble component at different RH levels for 1.6 μm.

	Soot	Water-soluble (RH=0%)	Water-soluble (RH=50%)	Water-soluble (RH=70%)
Real	1.778	1.53	1.411	1.391
Imaginary	0.468	0.00598	0.01093	0.00853
	Water-soluble (RH=80%)	Water-soluble (RH=90%)	Water-soluble (RH=95%)	Water
Real	1.376	1.357	1.344	1.317
Imaginary	0.00692	0.00476	0.00321	0.0000855

soot do not change with the increasing RH. Therefore, the volume fraction of the inclusions f in Eq. (3) for the MG rule can be given by

$$f=(R_{incl}/R_{drop})^3=1/\mathrm{GF}^3_{type\ \mathrm{I}} \tag{9}$$

Based on Eqs. (8) and (9), the scattering properties of five irregularly shaped type I particles as shown in Fig. 2 (a)–(e) (the spheroid with axial ratio $a/b=1$, 2; cylinder with diameter/height ratio $D/L=1$; Chebyshev particles with deformation parameter $\varepsilon=\pm0.1$ and polynomial of degree $n=2$) in 1.6 μm are simulated by combining the

T-matrix method with the MG rule. The mean and the coefficient of variation (CV, defined as the ratio of the standard deviation to the mean) of the scattering parameters for the above five shaped particles with the same equal-volume sphere radius are used to assess their sensitivity to shape parameters at different RH levels. Fig. 3 depicts the means and CVs of the scattering phase function (SPF) for different R_{incl} and RH, where the SPF hereinafter satisfies the normalization condition. As the RH increases, the scattering intensity increases in the forward scattering directions, while in the backward scattering directions it tends to roughly decrease. For small particles with R_{incl}=0.2 and 0.5 μm, the CVs are rather small both in the forward and middle scattering regions (0–120°), indicating the difference of the SPFs among five shaped particles is small (Fig. 3(a) and (b)). However, the CV becomes much larger when R_{incl} grows, and for R_{incl}=2.0 μm, it even exceeds 100% in the scattering angles between 20° and 40° (in the black box in Fig. 3(d)). In general, the CV at a high RH is relatively larger than that at a low RH, suggesting the impact of RH on the SPF is also related to the shape, particularly for larger particles when RH is high.

Tables 3 and 4 show the means and CVs of the extinction cross section (C_{ext}), scattering cross section (C_{sca}), absorption cross section (C_{abs}), single scattering albedo (ω) and asymmetry factor (g) of the above five shaped particles with R_{incl}=0.5 and 2.0 μm, respectively. Due to the changes in R_{drop} and complex refractive index resulted from the hygroscopic growth of particles, there is a significant growth trend for C_{ext}, C_{sca} and C_{abs} with the increase of RH. In the case of R_{incl}=0.5 μm, the C_{ext}, C_{sca}, C_{abs} and R_{drop} at a RH of 95% are approximately 4, 7.5, 1 and 1.1 times larger than those under dry air condition (RH=0%). For the ω and g, they also slightly increase with RH, but such increase is much larger for smaller particles. For example, when the RH increases from 0% to 95%, the increases in the ω and g for R_{incl}=2.0 μm are ~0.01 and ~0.05, respectively, while they are ~0.34 and ~0.18 for R_{incl}=0.5 μm. According to the CVs in Tables 3 and 4, these five scattering parameters of type I particles are less sensitive to shape parameters as compared to RH, especially for particles with small-size inclusions (e.g. R_{incl}= 0.5 μm). The maximum CVs are 7%, 13%, 0.1%, 6%, 2% for C_{ext}, C_{sca}, C_{abs}, ω and g when R_{incl}=2.0 μm, respectively, and they are only 1.1%, 1.3%, 1.4%, 0.6% and 0.7% when R_{incl}=0.5 μm.

To evaluate the variation of scattering properties influenced by the water-soluble coatings, we calculated the ratios of scattering properties at a certain RH to the correspondingly homogeneous soot particles with the same R_{drop}. We noticed that the calculated ratios are similar to each other for the five shape cases, so, for simplification, only the results of Chebyshev particle with ε=0.1 and n=2 are given. As illustrated in Fig. 4, the differences of scattering property ratios are obvious for different R_{incl} and RH. Generally, the

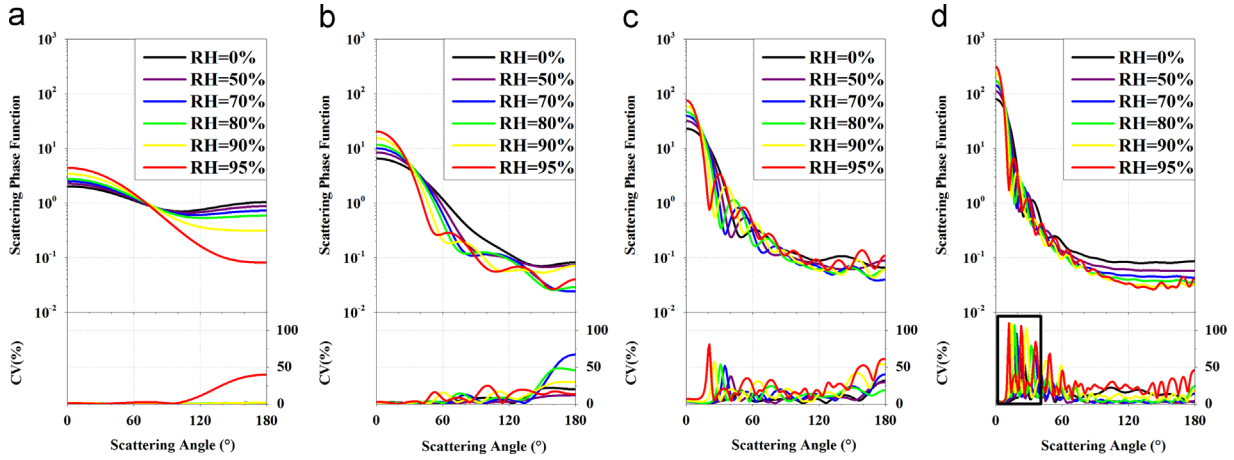

Fig. 3. Means (top panels) and CVs (bottom panels) for scattering phase functions of five irregularly shaped type I particles at eight RH levels. (a)–(d) with a R_{incl} of 0.2, 0.5, 1.0, and 2.0 μm, correspondingly.

Table 3
Means and CVs for the scattering properties of five shaped type I particles with R_{incl}=0.5 μm in 1.6 μm.

RH (%)	C_{ext} (μm^2)		C_{sca} (μm^2)		C_{abs} (μm^2)		ω		g	
	Mean	CV (%)	Mean	CV (%)	Mean	CV (%)	Mean	CV (%)	Mean	CV (%)
0	2.30	0.88	1.08	0.34	1.22	1.37	0.47	0.56	0.66	0.63
50	3.24	0.23	1.73	0.53	1.51	0.45	0.54	0.40	0.73	0.37
70	4.17	0.46	2.49	0.84	1.69	0.35	0.60	0.41	0.77	0.11
80	5.11	0.47	3.30	0.88	1.81	0.52	0.65	0.46	0.79	0.23
90	7.56	1.06	5.52	1.27	2.04	0.50	0.73	0.21	0.82	0.20
95	11.37	0.96	9.17	1.21	2.20	0.18	0.81	0.25	0.84	0.25

Table 4
Means and CVs for the scattering properties of five shaped type I particles with R_{incl}=2.0 μm in 1.6 μm.

RH (%)	C_{ext} (μm^2)		C_{sca} (μm^2)		C_{abs} (μm^2)		ω		g	
	Mean	CV (%)	Mean	CV (%)	Mean	CV (%)	Mean	CV (%)	Mean	CV (%)
0	32.98	6.97	17.14	12.39	15.84	0.03	0.52	5.39	0.88	1.44
50	44.28	3.80	21.99	3.87	22.29	0.04	0.50	0.17	0.91	0.16
70	56.72	3.77	28.10	3.92	28.62	0.04	0.50	0.17	0.92	0.29
80	69.15	3.70	34.43	3.98	34.72	0.03	0.50	0.35	0.93	0.39
90	96.96	3.75	49.57	4.31	47.39	0.03	0.51	0.58	0.94	0.46
95	133.64	4.66	71.18	6.22	62.46	0.03	0.53	1.71	0.93	0.59

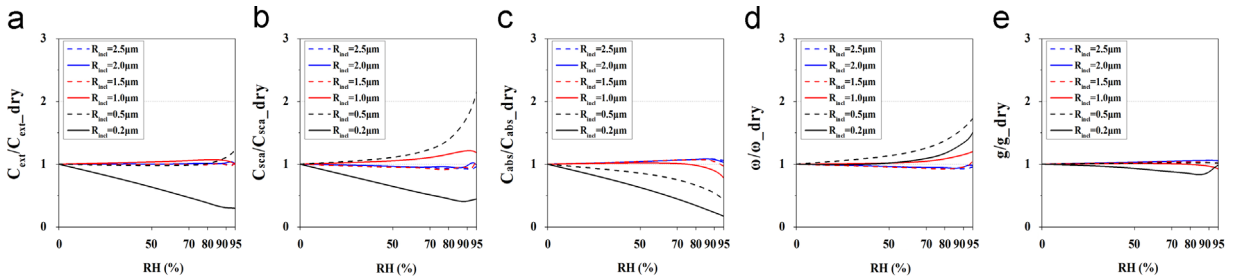

Fig. 4. Ratios of scattering properties of type I particles at a certain RH to the correspondingly homogeneous dry soot particles with the same R_{drop} for the case of Chebyshev particle (ε=0.1, n=2). (a)–(e) Ratios of C_{ext}, C_{sca}, C_{abs}, ω and g, correspondingly.

impact of water-soluble coatings for a small-size R_{incl} is stronger than that for a large-size R_{incl}, and is weaker for a low RH than that for a high RH. When R_{incl}=0.2 μm, if we only consider the hygroscopic growth in the simulation but neglect the heterogeneity of particles, the ω may be underestimated to ~50%, and the C_{ext}, C_{sca}, C_{abs} and g can be overestimated by ~70%, ~60%, ~90% and ~10%, respectively. With the increase of R_{incl}, the ratios of C_{ext}, C_{sca}, C_{abs}, ω and g all tend to oscillate around 1 at different RH. Therefore, the hygroscopic growth of inhomogeneous type I particles should be taken into account in the simulation of their optical properties, particularly for the haze/fog particles, because the haze/fog days are always associated with high levels of RH. Although the volume fraction of inclusion (soot), f, is fixed at a given RH, the scattering property ratios are different for different R_{incl} (or R_{drop}). Even though the particle with a small-size R_{incl} at a high RH can have the same R_{drop} as the one with a large-size R_{incl} at a low RH, their scattering property ratios are different, suggesting that both the size of inclusion and RH impact the variation of the scattering property ratios.

3.2. Soot aggregate with water-coated monomers (type II particle)

Because soot particles could support the surface tension of water as a film, soot aggregates frequently acquire water coatings in humid atmospheric environments. To some extent, the monomers always contact with each other loosely enough for water infiltration, so the type II particle can be assumed as a pure fractal-like aggregate, and each of its equal-size monomers is assumed to be a spherical soot particle with water coating. Some other forms of water coating that may be more realistic are beyond the scope of this paper. In moist air, the surface tension forces of water can reconstruct the particles by collapsing the loose constructs and ultimately forming a more dense globular shape (compact construct), and such shrinking and restructuring with elevated RH have been experimentally supported [55–58]. Here, the aggregate diameter is defined as the maximum projected length. D_p is the diameter of a humid soot aggregate (red double-sided arrows in Fig. 2), and D_0 is the diameter of the corresponding dry one. The core radius for each soot-containing monomer is fixed as a_{incl}=15 nm, a typical value for flame-generated soot. Therefore, for monomers in aggregates, observations from Khalizov (the diameter of dry soot particle D_0=30 nm) [58], Gysel (D_0=30 nm) [59] and D'Almeida [60] are used to fit the GF factors in Eq. (4) (dotted line in Fig. 5), and we got:

$$\mathrm{GF}_{type\ \mathrm{II},\ monomer} = a_{drop}/a_{incl} = \begin{cases} 1, & \mathrm{RH} \le 50\% \\ 0.934(1-\mathrm{RH}/100)^{-0.097}, & \mathrm{RH} > 50\% \end{cases} \quad (10)$$

For the soot aggregates, the values of k and D_f for freshly emitted soot aggregates are selected according to the study by Sorensen and Roberts [61], in which k=1.19 and D_f=1.82. Since the mean D_p of freshly aggregates with N=50 (based on 1000 cases) is ~360 nm, the GF model of soot aggregates (solid line in Fig. 5) is obtained by fitting the results of Khalizov (D_0=360 nm) [58] as follows:

$$\mathrm{GF}_{type\ \mathrm{II},\ aggregate} = D_p/D_0 = (1-\mathrm{RH}/100)^{0.163} \quad (11)$$

Using the sequential algorithm with Eq. (10), 1000 cases of aggregate with fixed N=50 and k=1.19 were generated for each value of D_f from 1.82 to 3 in steps of 0.01 and a certain level of RH from 0% to 95%. The D_f value for a certain level of RH can be obtained by matching the means of D_p to the calculated ones from Eq. (11). Finally, we got

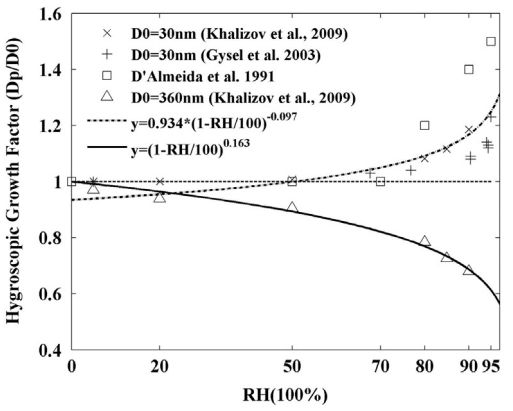

Fig. 5. Experimental results of hygroscopic growth factor of soot-containing aggregates for different D_0 and RH, and the fitted curves (D_0=30 and 360 nm).

D_f=1.82, 1.91, 2.09, 2.21, 2.43 and 2.7 for RH=0%, 50%, 70%, 80%, 90% and 95%, respectively.

In this paper, it is assumed that the D_f only changes with the RH, but does not change with N. Combining with the hygroscopic growth model of monomer, the sequential algorithm was used to generate the fractal aggregates composed of 50, 100 and 150 monomers with fixed k=1.19 and D_f ranged from 1.82 to 2.7 for the corresponding RH levels. The cases of type II particles with N=150 for the increasing RH are shown in Fig. 2(f)–(k). Then the CMGMM method was employed for calculating their scattering properties. Here, the complex refractive indices of both dry soot core and wet water coating are separate input parameters in the CMGMM method. Unlike type I particles, the SPFs of type II particles monotonically decrease with the RH in the forward scattering directions, and increase in the backward scattering directions, as shown in Fig. 6 (top row). The SPF is less affected by RH for smaller particles. However, the impact

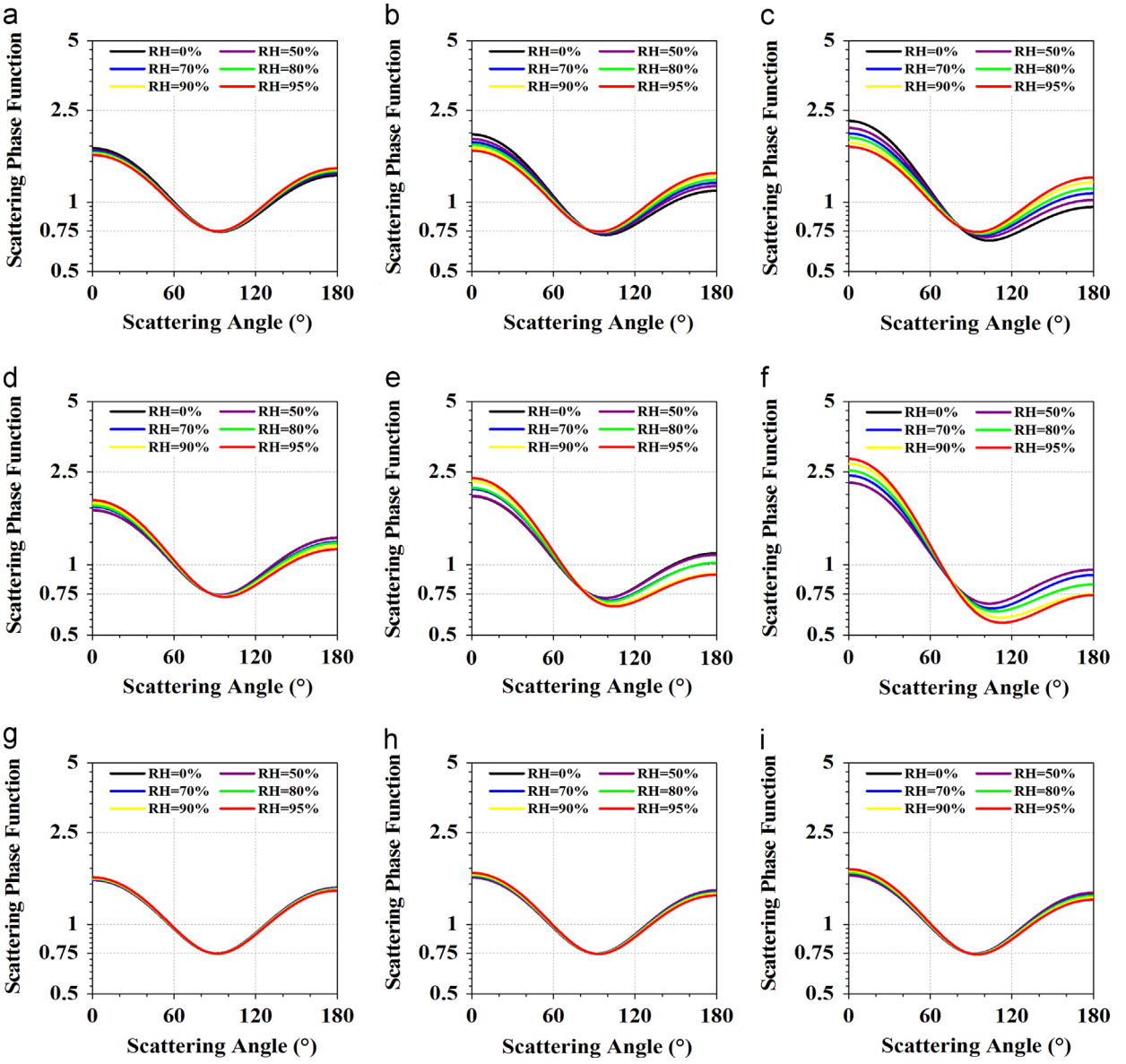

Fig. 6. Scattering phase functions of type II particles at different RH levels at 1.6 μm for k=1.19. The D_f values for top row are 1.82, 1.91, 2.09, 2.21, 2.43 and 2.7 for RH=0%, 50%, 70%, 80%, 90% and 95%, respectively. And D_f for middle and bottom rows are set fixed values 1.82 and 2.7, respectively. The monomer numbers for left, middle and right column are N=50, 100 and 150, respectively.

of RH becomes significant for larger particles, particularly in the forward scattering. To evaluate the impact of shape on type II particles, the scattering properties of fractal aggregates with fixed D_f=1.82 and 2.7 for different RH were also calculated. It is remarkable that the variation trend of SPFs with RH for a fixed D_f (Fig. 6(d)–(i)) is completely opposite to that for changed D_f (Fig. 6(a)–(c)), indicating that the shrink and restruction of type II particles with RH is one of the most critical factors influencing their scattering properties. If the increase of D_f with RH is ignored, the scattering intensity will be overestimated in the forward scattering, and underestimated in the backward scattering.

Fig. 7 reveals that the C_{ext}, C_{sca}, C_{abs} and ω of the type II particles with changed D_f increase with RH. And the impact of RH on the C_{ext}, C_{sca}, C_{abs} and ω for small particles (N=50) is smaller than that for relatively large particles (N=150). By comparing with corresponding results of soot-containing aggregates with fixed D_f=1.82 and 2.7 (blue and black solid lines in Fig. 7), it is evident that these scattering parameters will be underestimated if the impacts by RH and morphological changes are not taken into account. Taking the ω as an example, the ω for RH=95%, D_f=2.7 is as much as ~2 times of that for RH=0%, D_f=1.82 when N=150. With the increase of RH,

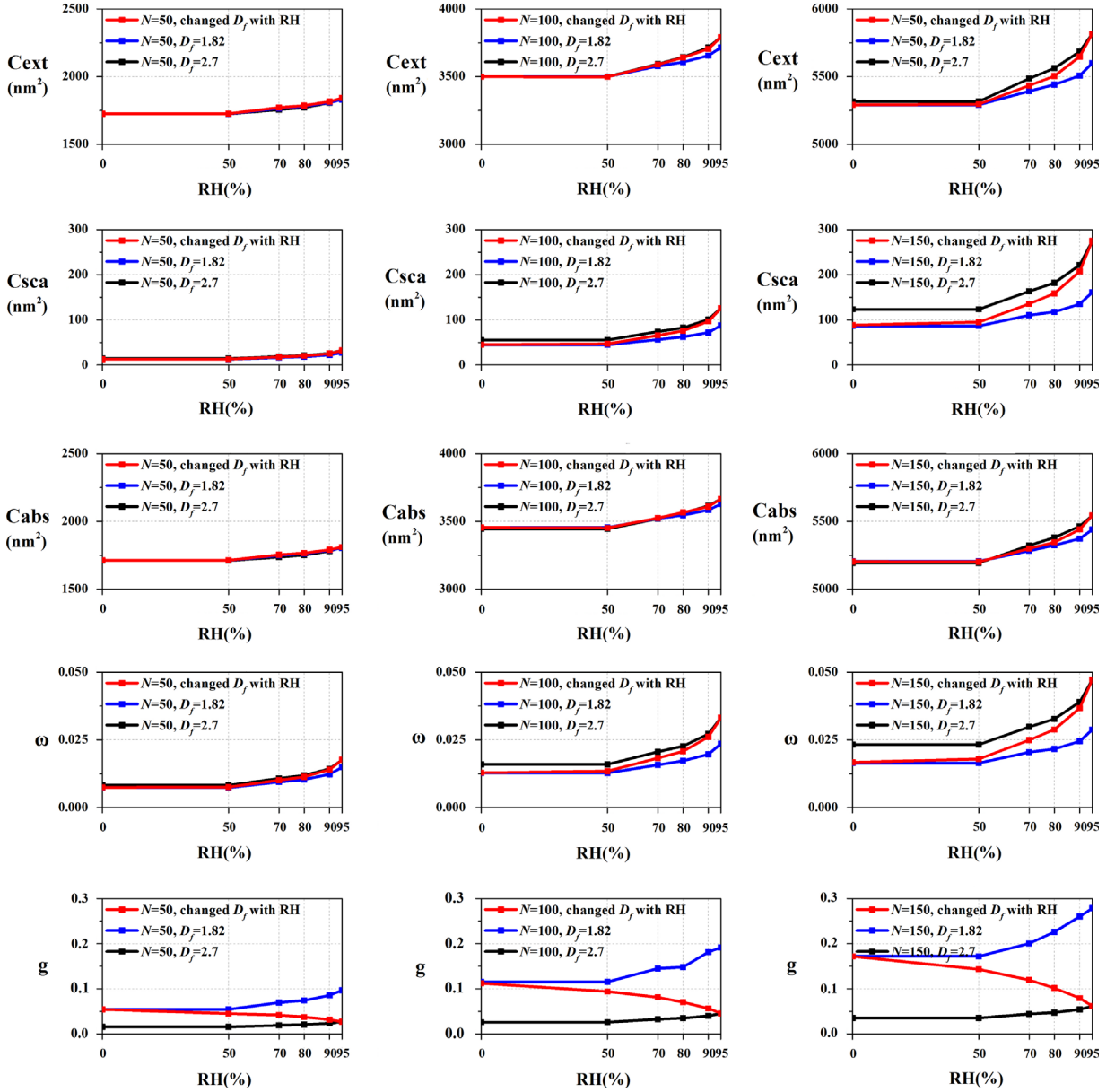

Fig. 7. The extinction cross section (top row), scattering cross section (second row), absorption cross section (third row), single scattering albedo (forth row) and asymmetry parameter (bottom row) of type II soot-containing particles with k=1.19 as the functions of RH at 1.6 μm. The monomer numbers for left, middle and right column are N=50, 100 and 150, respectively. (For interpretation of the references to color in this figure, the reader is referred to the web version of this article.)

g of type II particles decreases from 0.054 to 0.027 for $N=50$, and from 0.17 to 0.06 for $N=150$ resulted from the shape of soot aggregate changing from loose construct to compact construct. However, the g increases monotonically with RH for a fixed D_f. Overall, the scattering properties of type II particles are primarily impacted by the RH, followed by the morphology. The impact of morphology should not be neglected for a high RH.

The ratios of scattering properties of type II particles with changed D_f to those of corresponding aggregates composed of homogeneous soot monomers with the same size and morphology are shown in Fig. 8. The ratios of C_{ext}, C_{sca} and C_{abs} reduce significantly as the RH increases, but they are almost insensitive to the particle size at a fixed RH (Fig. 8(a)–(c)). All of these three parameters reach to about 0.4 when RH=95%. The ratio of ω has a positive relation to the size, and decreases with RH while RH is less than 90% but increase when RH is larger than 90% (Fig. 8(d)). The ratios of g are all larger than 0.95 for RH between 0% and 95%, suggesting that they are nearly unaffected by both the RH and N (Fig. 8(e)). Although the equal-volume radii of the type II soot-containg aggregates are always quite small, the ratio changes for type II particles are not entirely similar to type I particles with small-size R_{incl} (e.g. R_{incl}= 0.2 μm in Fig. 4), especially for ω.

3.3. Soot aggregate semi-externally mixed with large water-soluble particle (type III particle)

For simplicity, it is assumed that the soot aggregate of a type III particle (Fig. 2(l)) has the same chemical, physical and morphological properties with the type II aggregates studied in Section 3.2, and the extra particle is only composed of homogeneous water-soluble material. The GF model of extra particle obeys Eq. (8), and the models of the soot aggregate and its monomers follow Eqs. (11) and (10), respectively. Here, the radius of dry core of the extra particle for RH 0% is denoted as $R_{other,\ dry}$. Similar to type II particle, the cases of soot aggregate ($N=50$, 100, 150, $k_f=1.19$ and the changed D_f with RH) semi-externally mixed with large particle ($R_{other,\ dry}=0.2$ and 0.5 μm) are generated by the sequential algorithm, and their scattering properties are calculated by combining the CMGMM method and the hygroscopic growth theory. For comparison, the scattering properties of exclusively water-soluble extra particles are also simulated. Because the scattering properties of soot aggregates attached to extra particles with different shapes are similar to each other, only the results of soot aggregate attached to Chebyshev particle ($\varepsilon=0.1$ and $n=2$) are given. According to Fig. 9, the larger value of $R_{other,\ dry}$ leads to higher scattering intensities in the forward scattering, and smaller in the backward scattering. It is notable that the angular dependence of SPF of the type III particle with $N=150$ is very similar to that for pure water-soluble extra particle. This means that the soot aggregate attached to an extra particle has little effect on the SPF, and the direction of light will not be strikingly changed by the type III particles with different number of N (from 50 to 150, or even large).

Comparison of scattering parameters of type III particles with $N=150$, $R_{other,\ dry}=0.2$ and 0.5 μm (Fig. 10, the top panels) shows that the elevated RH leads to larger differences in C_{ext}, C_{sca} and C_{abs} among different type III particles with different $R_{other,\ dry}$, while the differences in ω and g become smaller. By subtracting the scattering parameters of type III particles with $N=100$, 50 and 0 from those of the

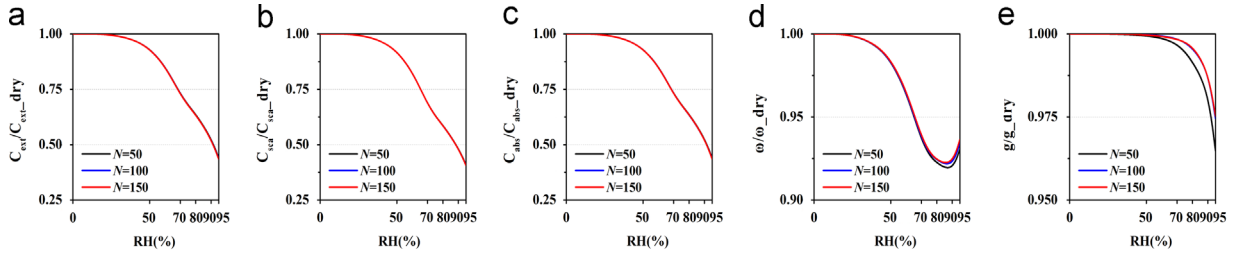

Fig. 8. Ratios of scattering properties of type II particles at a certain RH to the corresponding dry aggregates composed of homogeneous soot monomers with the same size and morphology. (a)–(e) Ratios of C_{ext}, C_{sca}, C_{abs}, ω and g, correspondingly.

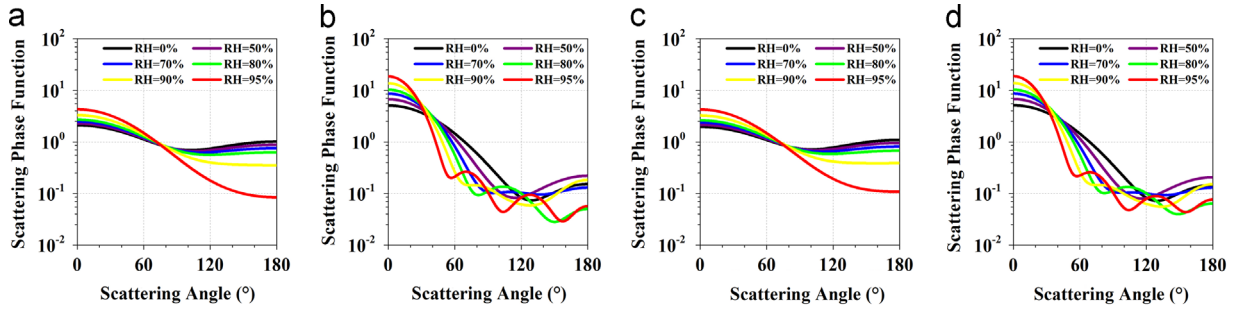

Fig. 9. (a) and (b) Scattering phase functions of soot aggregate ($N=150$, $k_f=1.19$ and changed D_f with RH) semi-externally mixed with water-soluble Chebyshev particle ($\varepsilon=0.1$ and $n=2$) at different RH levels for $R_{other,\ dry}=0.2$ and 0.5 μm, respectively. (c) and (d) Scattering phase functions of the water-soluble Chebyshev particle ($\varepsilon=0.1$ and $n=2$) for $R_{other,\ dry}=0.2$ and 0.5 μm, respectively.

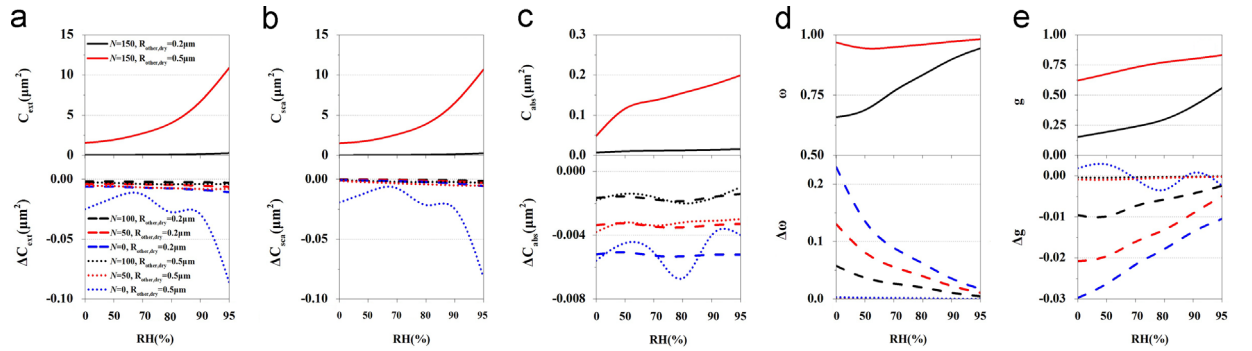

Fig. 10. Scattering parameters of soot aggregates semi-externally mixed with water-soluble Chebyshev particle (ε=0.1 and n=2) for N=150, $R_{other,\ dry}$=0.2 and 0.5 μm at 1.6 μm (top panels). And the differences in scattering parameters between type III particles with N=100/50/0 and the corresponding ones with N=150 and the same $R_{other,\ dry}$ (bottom panels).

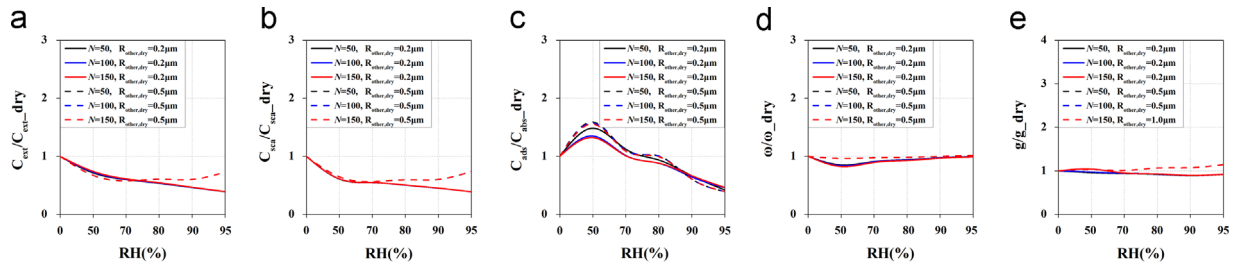

Fig. 11. Ratios of scattering properties of soot aggregates semi-externally mixed with water-soluble Chebyshev particles (ε=0.1 and n=2) at a certain RH to the correspondingly dry particles with the same N, morphology and the radius of extra water-soluble particles. (a)–(e) Ratios of C_{ext}, C_{sca}, C_{abs}, ω and g, correspondingly.

corresponding ones with N=150 and the same $R_{other,\ dry}$, as shown in Fig. 10 (bottom panels), we can see that for $R_{other,\ dry}$=0.2 μm, the soot-containing aggregate mainly impacts C_{ext}, C_{sca} and C_{abs} of the entire type III particle. However, for $R_{other,\ dry}$=0.5 μm, the aggregate mainly impacts the ω and g. Given a fixed $R_{other,\ dry}$, the C_{ext}, C_{sca}, C_{abs} and g are enhanced by the increasing N, but the ω is declined. Generally, variation of $R_{other,\ dry}$ plays a much more prominent role in influencing the scattering properties of the entire mixture than the change of N at a fixed RH level, which is consistent with the study of Liu and Mishchenko [62]. From Fig. 10 we can see that under the condition of RH=95% and N=150, when $R_{other,\ dry}$ increases from 0.2 to 0.5 μm, C_{ext}, C_{sca} and C_{abs} increase by 10.6 μm^2, 10.4 μm^2 and 0.2 μm^2, respectively. In contrast, under the condition of $R_{other,\ dry}$=0.2 μm, when N increases from 50 to 150, they increase only by 0.006 μm^2, 0.003 μm^2 and 0.003 μm^2. Although N almost does not impact the ω when $R_{other,\ dry}$=0.5 μm, it should be noted that when the size of extra water-soluble particle is small (i.e. $R_{other,\ dry}$=0.2 μm), the striking reduction of ω (~0.15) by the enlarged soot aggregates at low RH may lead to a large error in CO_2 retrieval.

As shown in Fig. 11, the ratios of C_{ext}, C_{sca} and C_{abs} for type III particles relative to their corresponding dry ones are mainly impacted by RH and $R_{other,\ dry}$, followed by N. The effect of N is almost ignorable for larger particles, except for C_{abs}. For small particles ($R_{other,\ dry}$=0.2 μm), the C_{ext}, C_{sca} and C_{abs} of the entire individual III particles are significantly smaller than the corresponding dry ones, especially at a high RH. However, for large particles ($R_{other,\ dry}$=0.5 μm), the C_{ext} and C_{sca} are enhanced at high levels of RH, while the C_{abs} is enhanced at low levels of RH. The ratios of ω and g are barely impacted by RH and the morphology of particles. Overall, both the water coatings of soot aggregates and the chemical properties of the extra water-soluble particles significantly impacted the scattering properties of type III particles, and the specific impact mainly depends on the sizes of extra particles.

4. Summary and conclusion

Based upon previous aerosol observations during haze events in China, there are three typical types of soot-containing particles grouped in this study: internal mixtures (type I), pure soot aggregates (type II) and semi-external mixtures (type III). Their scattering properties in 1.6 μm were investigated by using the T-matrix method and the CMGMM method combined with the effective medium rule, the hygroscopic growth theory, and the particle-cluster aggregation algorithm, with a focus on their impact by RH. Here, not only the growth of the single particles and the growth of monomers with RH were considered in the hygroscopic growth, but the shrinking and restruction of the aggregates with RH were also investigated. According to the simulated results, some characteristics of the scattering properties variation are found:

(1) The scattering properties are significantly different among these three types of aerosols at different levels

of RH. Generally, the impacts of both the morphology and the size of inclusions on their scattering properties are larger at a higher RH.

(2) For the type I particles, the SPF grows up with the increase of RH in the forward scattering directions, and a large difference in SPF resulted from shapes occurred to a large particle with a high RH. All of the C_{ext}, C_{sca}, C_{abs}, ω and g nearly increase at an elevated level of RH. However, the increments of the C_{ext}, C_{sca} and C_{abs} for small particle are much smaller than those for relatively large one. For $R_{incl}=2.0$ μm, the CVs of C_{ext}, C_{sca}, C_{abs}, ω and g among five shaped particles are less than 7%, 13%, 0.1%, 6%, and 2%, respectively, suggesting that the RH has a much larger impact than shapes.

(3) For the type II particles, both the RH and the morphology play important roles in the variation of scattering characteristics. In contrast to the type I particles, the SPF of type II decreases with the RH in the forward scattering, and increases in the backward scattering. When the morphology of aggregated particle exposed to the elevated RH transforms from loose to compact structure, the backward scattering intensities, C_{ext}, C_{sca}, C_{abs} and ω increase while the forward scattering intensities and g decrease. The ω can be obviously underestimated by up to 50% if the impact of RH on the morphology is not taken into account.

(4) For the type III particles, the size of water-soluble particle that is in touch with soot aggregate can strongly influence, or even dominate, the overall optical characteristics of the mixture at a fixed RH level. The increasing RH leads larger differences in C_{ext}, C_{sca} and C_{abs} among type III particles with same N but different $R_{other,\ dry}$, but leads smaller differences in both ω and g. Although the scattering properties are almost insensitive to the size of soot aggregate for large particles, it should be notable that a significant reduction of ω by the enlarged soot aggregates can be up to ~0.15 at low RH when the size of extra water-soluble particle is small.

(5) Comparison of the scattering parameters for soot-containing particles at a certain RH level with the corresponding particles with the same size and morphology in dry air shows that the heterogeneity of particles could introduce large differences in the scattering properties. Overall, the differences are larger for smaller particles and higher RH levels, and they are very small among particles with different morphologies.

Although the water vapor absorption is very weak near the spectra of 1.6 μm CO_2 band, RH could significantly influence the scattering properties of aerosol particles through the hygroscopic growth and the change of effective particle compositions. These results suggest that the effect of water vapor on the aerosols should be taken into account in the CO_2 retrieval, and other remote sensing applications.

Acknowledgments

The authors appreciate financial support for this work from the Key Program of the National Natural Science Foundation of China (Grant no. 41130528) and the Strategic Priority Research Program of the Chinese Academy of Sciences (Grant no. XDB05020100). We thank Dr. Michael I. Mishchenko for publicly providing the T-matrix code (http://www.giss.nasa.gov/staff/mmishchenko/t_matrix.html), and thank Dr. Yunlin Xu for publicly providing the CMGMM code (http://www.scattport.org/files/xu/codes.htm).

References

[1] Chevallier F, Bréon F-M, Rayner PJ. Contribution of the Orbiting Carbon Observatory to the estimation of CO_2 sources and sinks: theoretical study in a variational data assimilation framework. J Geophys Res 2007;112(D9):D09307.
[2] Meirink JF, Eskes HJ, Goede APH. Sensitivity analysis of methane emissions derived from SCIAMACHY observations through inverse modelling. Atmos Chem Phys 2006;6(5):1275–92.
[3] Kuang Z, Margolis J, Toon G, Crisp D, Yung Y. Spaceborne measurements of atmospheric CO_2 by high-resolution NIR spectrometry of reflected sunlight: an introductory study. Geophys Res Lett 2002;29(11-1–11-4).
[4] Christi MJ, Stephens GL. Retrieving profiles of atmospheric CO_2 in clear sky and in the presence of thin cloud using spectroscopy from the near and thermal infrared: a preliminary case study. J Geophys Res 2004;109(D4):D04316.
[5] Crisp D, Atlas RM, Breon FM, Brown LR, Burrows JP, Ciais P, et al. The Orbiting Carbon Observatory (OCO) mission. Adv Space Res 2004;34(4):700–9.
[6] Dufour E, Bréon F-M. Spaceborne estimate of atmospheric CO_2 column by use of the differential absorption method: error analysisjournal of quantitative spectroscopy and radiative transfer. Appl Opt 2003;42:3595–609.
[7] Mao J, Kawa SR. Sensitivity studies for space-based measurement of atmospheric total column carbon dioxide by reflected sunlight. Appl Opt 2004;43:914–27.
[8] Aben I, Hasekamp O, Hartmann W. Uncertainties in the space-based measurements of CO_2 columns due to scattering in the Earth's atmosphere. J Quant Spectrosc Radiat Transfer 2007;104(3):450–9.
[9] Li Z, Chen H, Cribb M, Dickerson R, Holben B, Li C, et al. Preface to special section on East Asian Studies of tropospheric aerosols: an International Regional Experiment (EAST-AIRE). J Geophys Res 2007;112(D22):D22S00.
[10] Streets DG, Yu C, Wu Y, Chin M, Zhao Z, Hayasaka T, et al. Aerosol trends over China, 1980–2000. Atmos Res 2008;88(2):174–82.
[11] Che H, Zhang X, Li Y, Zhou Z, Qu J, Hao X. Haze trends over the capital cities of 31 provinces in China, 1981–2005. Theor Appl Climatol 2009;97(3):235–42.
[12] Tang IN. Chemical and size effects of hygroscopic aerosols on light scattering coefficients. J Geophys Res 1996;101(D14):19245–50.
[13] Markowicz KM, Flatau PJ, Quinn PK, Carrico CM, Flatau MK, Vogelmann AM, et al. Influence of relative humidity on aerosol radiative forcing: an ACE-Asia experiment perspective. J Geophys Res 2003;108(D23):8662.
[14] Ram K, Sarin MM, Sudheer AK, Rengarajan R. Carbonaceous and secondary inorganic aerosols during wintertime fog and haze over urban sites in the Indo-Gangetic plain. Aerosol Air Qual Res 2012;12:359–70.
[15] Zhang XY, Wang YQ, Niu T, Zhang XC, Gong SL, Zhang YM, et al. Atmospheric aerosol compositions in China: spatial/temporal variability, chemical signature, regional haze distribution and comparisons with global aerosols. Atmos Chem Phys 2012;12(2):779–99.
[16] Kaufman YJ, Tanré D, Remer LA, Vermote EF, Chu A, Holben BN. Operational remote sensing of tropospheric aerosol over land from EOS moderate resolution imaging spectroradiometer. J Geophys Res: Atmos 1997;102(D14):17051–67.
[17] Buseck PR. Atmospheric-particle research; past, present, and future. Elements 2010;6(4):208–9.
[18] Li W, Shao L. Transmission electron microscopy study of aerosol particles from the brown hazes in northern China. J Geophys Res 2009;114(D9):D09302.
[19] Li WJ, Shao LY. Observation of nitrate coatings on atmospheric mineral dust particles. Atmos Chem Phys 2009;9(6):1863–71.
[20] Li WJ, Shao LY, Buseck PR. Haze types in Beijing and the influence of agricultural biomass burning. Atmos Chem Phys 2010;10(17):8119–30.

[21] Li WJ, Zhang DZ, Shao LY, Zhou SZ, Wang WX. Individual particle analysis of aerosols collected under haze and non-haze conditions at a high-elevation mountain site in the North China plain. Atmos Chem Phys 2011;11(22):11733–44.
[22] Waterman PC. Matrix formulation of electromagnetic scattering. Proc IEEE 1965;53(8):805–12.
[23] Mishchenko MI, Travis LD, Mackowski DW. T-matrix computations of light scattering by nonspherical particles: a review. J Quant Spectrosc Radiat Transfer 1996;55(5):535–75.
[24] Mishchenko MI, Travis LD. Capabilities and limitations of a current FORTRAN implementation of the T-matrix method for randomly oriented, rotationally symmetric scatterers. J Quant Spectrosc Radiat Transfer 1998;60(3):309–24.
[25] Mishchenko MI. Calculation of the amplitude matrix for a nonspherical particle in a fixed orientation. Appl Opt 2000;39(6):1026–31.
[26] Yang P, Liou KN. Light scattering by hexagonal ice crystals: comparison of finite-difference time domain and geometric optics models. J Opt Soc Am A 1995;12(1):162–76.
[27] Sun W, Fu Q, Chen Z. Finite-difference time-domain solution of light scattering by dielectric particles with a perfectly matched layer absorbing boundary condition. Appl Opt 1999;38(15):3141–51.
[28] Purcell EM, Pennypacker CR. Scattering and absorption of light by nonspherical dielectric grains. Astrophys J 1973;186:705–14.
[29] Koylu UO, Faeth GM. Optical properties of overfire soot in buoyant turbulent diffusion flames at long residence times. J Heat Transfer 1994;116(1):152–9.
[30] Mulholland GW, Bohren CF, Fuller KA. Light scattering by agglomerates: coupled electric and magnetic dipole method. Langmuir 1994;10(8):2533–46.
[31] Bruning J, Lo Y. Multiple scattering of EM waves by spheres part I—multipole expansion and ray-optical solutions. IEEE Trans Antennas Propag 1971;19(3):378–90.
[32] Bruning J, Lo Y. Multiple scattering of EM waves by spheres part II—numerical and experimental results. IEEE Trans Antennas Propag 1971;19(3):391–400.
[33] Mishchenko MI. Light scattering by randomly oriented axially symmetric particles. J Opt Soc Am A 1991;8(6):871–82.
[34] Khlebtsov NG. Orientational averaging of light-scattering observables in the T-matrix approach. Appl Opt 1992;31(25):5359–65.
[35] Xu YL. Electromagnetic scattering by an aggregate of spheres. Appl Opt 1995;34(21):4573–88.
[36] Xu YL. Electromagnetic scattering by an aggregate of spheres: far field. Appl Opt 1997;36(36):9496–508.
[37] Xu YL, Khlebtsov NG. Orientation-averaged radiative properties of an arbitrary configuration of scatterers. J Quant Spectrosc Radiat Transfer 2003;79–80(0):1121–37.
[38] Garnett JMC. Colours in metal glasses and in metallic films. Philos Trans R Soc London 1904;203(359–371):385–420.
[39] Garnett JMC. Colours in metal glasses, in metallic films, and in metallic solutions. II. .Philos Trans R Soc London 1906;205:237–88.
[40] Bruggeman DAG. Calculation of various physics constants in heterogenous substances. I: Dielectricity constants and conductivity of mixed bodies from isotropic substances. Ann Phys 1935;24(7):636–64.
[41] Landauer R. Electrical conductivity in inhomogeneous media. AIP Conf Proc 1978;40(1):2–45.
[42] Soven P. Coherent-potential model of substitutional disordered alloys. Phys Rev 1967;156(3):809–13.
[43] Velický B, Kirkpatrick S, Ehrenreich H. Single-site approximations in the electronic theory of simple binary alloys. Phys Rev 1968;175(3):747–66.
[44] Liu C, Panetta RL, Yang P. The influence of water coating on the optical scattering properties of fractal soot aggregates. Aerosol Sci Technol 2011;46(1):31–43.
[45] Forrest SR, Witten Jr. TA. Long-range correlations in smoke-particle aggregates. J Phys A 1979;12(5):L109.
[46] Filippov AV, Zurita M, Rosner DE. Fractal-like aggregates: relation between morphology and physical properties. J Colloid Interface Sci 2000;229(1):261–73.
[47] Swietlicki E, Zhou J, Covert DS, Hämeri K, Busch B, Väkeva M, et al. Hygroscopic properties of aerosol particles in the north-eastern Atlantic during ACE-2. Tellus B 2000;52(2):201–27.
[48] Peng C, Chan MN, Chan CK. The hygroscopic properties of dicarboxylic and multifunctional acids: measurements and UNIFAC predictions. Environ Sci Technol 2001;35(22):4495–501.
[49] Weingartner E, Gysel M, Baltensperger U. Hygroscopicity of aerosol particles at low temperatures. 1. New low-temperature H-TDMA instrument: setup and first applications. Environ Sci Technol 2001;36(1):55–62.
[50] Maßling A, Wiedensohler A, Busch B, Neusüß C, Quinn P, Bates T, et al. Hygroscopic properties of different aerosol types over the Atlantic and Indian Oceans. Atmos Chem Phys 2003;3(5):1377–97.
[51] Gysel M, Weingartner E, Nyeki S, Paulsen D, Baltensperger U, Galambos I, et al. Hygroscopic properties of water-soluble matter and humic-like organics in atmospheric fine aerosol. Atmos Chem Phys 2004;4(1):35–50.
[52] Hess M, Koepke P, Schult I. Optical properties of aerosols and clouds: the software package OPAC. Bull Am Meteorol Soc 1998;79(5):831–44.
[53] Rothman LS, Gordon IE, Barbe A, Benner DC, Bernath PF, Birk M, et al. The HITRAN 2008 molecular spectroscopic database. J Quant Spectrosc Radiat Transfer 2009;110:533–72.
[54] Hänel G. The size of atmospheric aerosol particles as a function of the relative humidity. Beitr Phys Atmos 1970;43:119–32.
[55] Weingartner E, Burtscher H, Baltensperger U. Hygroscopic properties of carbon and diesel soot particles. Atmos Environ 1997;31(15):2311–27.
[56] Mikhailov EF, Vlasenko SS, Podgorny IA, Ramanathan V, Corrigan CE. Optical properties of soot-water drop agglomerates: an experimental study. J Geophys Res 2006;111(D7):D07209.
[57] Mikhailov EF, Vlasenko SS. Structure and optical properties of soot aerosol in a moist atmosphere: 1. Structural changes of soot particles in the process of condensation. Izv, Atmos Ocean Phys 2007;43(2):181–94.
[58] Khalizov AF, Zhang R, Zhang D, Xue H, Pagels J, McMurry PH. Formation of highly hygroscopic soot aerosols upon internal mixing with sulfuric acid vapor. J Geophys Res 2009;114(D5):D05208.
[59] Gysel M, Nyeki S, Weingartner E, et al. Properties of jet engine combustion particles during the PartEmis experiment. Hygroscopic growth at supersaturated conditions. Geophys Res Lett 2003;30(14):1779.
[60] d'Almeida GA, Koepke P, Shettle EP. Atmospheric aerosols: global climatology and radiative characteristics. Hampton, VA: A. Deepak Publications; 1991.
[61] Sorensen CM, Roberts GC. The prefactor of fractal aggregates. J Colloid Interface Sci 1997;186(2):447–52.
[62] Liu L, Mishchenko MI. Scattering and radiative properties of complex soot and soot-containing aggregate particles. J Quant Spectrosc Radiat Transfer 2007;106(1–3):262–73.